

Measuring the Temperature of Extremely Hot Shock-Heated Gas in the Major Merger MACS J0717.5+3745 With Relativistic Corrections to the Sunyaev-Zel'dovich Effect

BENJAMIN J. VAUGHAN ^{1,2} JACK SAYERS ³ LOCKE SPENCER ⁴ NICHOLAS SWIDINKSI,⁴ RYAN WILLS ¹
MICHAEL ZEMCOV ^{1,5} DEREK ARTHUR,⁴ VICTORIA BUTLER ² RICHARD M. FEDER ^{6,7} DANIEL KLYDE ¹
LORENZO LOVISARI ^{8,9} ADAM MANTZ ¹⁰ AND EMILY M. SILICH ³

¹*Rochester Institute of Technology 1 Lomb Memorial Drive Rochester, NY 14623, USA*

²*Cornell University 109 Clark Hall Ithaca, NY 14850, USA*

³*California Institute of Technology 1200 E California Blvd Pasadena, CA 91125, USA*

⁴*University of Lethbridge 4401 University Dr W, Lethbridge, AB T1K 3M4, Canada*

⁵*Jet Propulsion Laboratory 4800 Oak Grove Drive Pasadena, CA 91109, USA*

⁶*Berkeley Center for Cosmological Physics, University of California, Berkeley, CA 94720, USA*

⁷*Lawrence Berkeley National Laboratory, Berkeley, California 94720, USA*

⁸*INAF, Istituto di Astrofisica Spaziale e Fisica Cosmica, Via Alfonso Corti 12, 20133 Milano, Italy*

⁹*Center for Astrophysics | Harvard & Smithsonian, 60 Garden St., Cambridge, MA 02138, USA*

¹⁰*Kavli Institute for Particle Astrophysics and Cosmology, Stanford University, 452 Lomita Mall, Stanford, CA 94305, USA*

ABSTRACT

The conversion of gravitational potential to kinetic energy results in an intracluster medium (ICM) gas with a characteristic temperature near 10 keV in the most massive galaxy clusters. X-ray observations, primarily from *Chandra* and *XMM-Newton*, have revealed a wealth of information about the thermodynamics of this gas. However, two regimes remain difficult to study with current instruments: superheated gas well above 10 keV generated by shocks from major mergers, and distant systems strongly impacted by cosmological dimming. Relativistic corrections to the Sunyaev-Zel'dovich effect (rSZe) produce a fractional spectral distortion in the cosmic microwave background at sub-millimeter and millimeter wavelengths that could offer a complimentary probe of both high temperature and high redshift ICM gas. Here we describe multi-band measurements of the rSZe, including observations from the Fourier Transform Spectrometer on the *Herschel*-SPIRE instrument, that constrain the ICM thermodynamics of the major merger MACS J0717.5+3745. Within the seven observed lines of sight, we find an average temperature of $T_{\text{rSZe}} = 15.1^{+3.8}_{-3.3}$ keV, which is consistent with the values obtained from X-ray measurements of the same regions, with $T_{\text{Chandra}} = 18.0^{+1.1}_{-1.1}$ keV and $T_{\text{XMM}} = 13.9^{+0.9}_{-0.9}$ keV. This work demonstrates that the rSZe signal can be detected with moderate spectral resolution sub-millimeter data, while also establishing the utility of such measurements for probing superheated regions of the ICM.

Keywords: Sunyaev-Zeldovich effect(1654) — Cosmology(343) — Galaxy Clusters(584) — Extragalactic Astronomy(506) — Intracluster Medium(858) — X-ray Astronomy(1810) — galaxies: clusters: individual: MACS J0717.5+3745

1. INTRODUCTION

The intracluster medium (ICM) comprises approximately 15 per cent of the total mass and approximately 85 per cent of the baryonic mass of galaxy clusters (Gonzalez et al. 2007; Lin et al. 2012), making the ICM an

important and dynamic constituent in these systems. Direct observations of the structure and thermodynamics of the ICM are critical to understanding the evolution of clusters and their relationship to the underlying dark matter distribution over cosmic time. In the most massive objects ($M \simeq 10^{15} M_{\odot}$), the ICM can be heated to temperatures near 10^8 K ($kT \simeq 10$ keV) through conversion from potential to kinetic energy as matter accretes

onto the cluster (Kravtsov & Borgani 2012). Additionally, major mergers drive shocks that can heat regions of the ICM to much higher temperatures, with $kT_{\text{ICM}} \simeq 40$ keV inferred in extreme systems (e.g., Markevitch 2006; Markevitch & Vikhlinin 2007).

The ICM is primarily observed using X-rays where the hot gas emits directly via thermal Bremsstrahlung continuum and line emission (e.g., Birzan et al. 2004; Vikhlinin et al. 2006; Markevitch & Vikhlinin 2007; Cavagnolo et al. 2009; Arnaud et al. 2010). A spectral fit of this emission permits inference of the electron temperature, T_e (e.g., Sarazin 1986; Schellenberger et al. 2015). However, X-ray instruments are typically optimized for energy bands below the highest temperatures expected in the ICM, with sensitivity dropping rapidly by $E \simeq 8$ keV for both *XMM-Newton* (Jansen et al. 2001) and *Chandra* (Weisskopf et al. 2000). While not traditionally utilized for ICM studies, X-ray facilities such as *NuStar* do have the capability to observe photon energies up to 50 keV (Harrison et al. 2013), but challenges related to its broad point spread function (PSF) and small collecting area limit its ability to measure ICM temperatures (e.g., Wik et al. 2014). As a result of these instrumental limitations, regions of particularly hot gas in major mergers are challenging to characterize via X-rays, which is further compounded by Cosmological dimming in high redshift clusters (e.g., Calzadilla et al. 2024). There is strong motivation to develop alternative ways to measure the temperature of the ICM.

The Sunyaev-Zeldovich effect (SZe) offers a probe of ICM thermodynamics that is independent of and complementary to X-ray observations (Mroczkowski et al. 2019; Lee et al. 2022). The SZe is the spectral distortion in the cosmic microwave background (CMB) radiation caused by inverse-Compton scattering of cold $T_{\text{CMB}} = 2.73$ K photons from energetic ICM electrons (Sunyaev & Zeldovich 1972; Birkinshaw 1999). For a stationary plasma, the effect is dependent on the thermal properties of the gas (tSZ), and can be modeled as an intensity shift in the CMB spectrum described by:

$$\Delta I_{\text{tSZ}} = I_0 \frac{x^4 e^x}{(e^x - 1)^2} \left(x \frac{e^x + 1}{e^x - 1} - 4 \right) \times (1 + \delta(x, T_e)) \int n_e \frac{kT_e}{m_e c^2} \sigma_T dl, \quad (1)$$

where $I_0 = \frac{2(kT_{\text{CMB}})^3}{(hc)^2}$ and $x \equiv \frac{h\nu}{kT_{\text{CMB}}}$ (Carlstrom et al. 2002). The term expressing an integral along the line-of-sight gives the Compton y parameter, which indicates the average energy boost to a CMB photon as a proportion of the electron rest mass. The ICM is sufficiently hot that mild relativistic corrections to the classical scattering are required to fully describe the intensity spec-

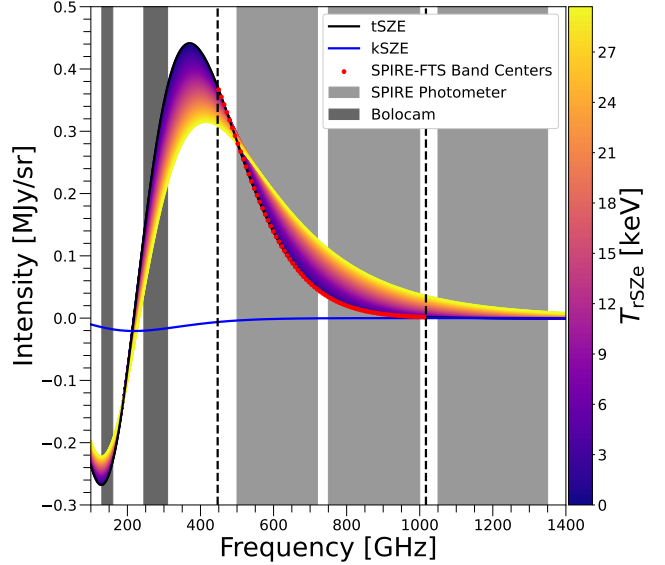


Figure 1. The spectrum of each component of the SZe for a range of T_{rSZe} calculated from *SZPack* (Chluba et al. 2012, 2013) assuming a Comptonization $y = 2.4 \times 10^{-4}$ and a peculiar velocity of 800 km s^{-1} . Dark grey regions denote the observing bands of Bolocam (Glenn et al. 2003) and red points indicate the band centers of the SPIRE-FTS, both of which are utilized to fit the SZe spectrum in our analysis. Also shown as light grey regions are the observing bands of the *Herschel*-SPIRE photometer (Valtchanov 2018), which are used to estimate the contaminating signal from thermal dust emission.

trum (Wright 1979). These corrections can be included in the term $\delta(x; T_e)$, a modification that is often referred to as the relativistic correction (rSZ), Itoh et al. 1998; Chluba et al. 2012, 2013; Remazeilles & Chluba 2025; Remazeilles 2022). A kinematic effect (kSZ) is also present due to coherent bulk velocities of and in the ICM material along the line of sight, and is modeled by:

$$\Delta I_{\text{kSZ}} = -I_0 \frac{x^4 e^x}{(e^x - 1)^2} y (1 + \delta(x, v_{\text{pec}}, T_e)). \quad (2)$$

The spectra of both the thermal and kinematic effects are plotted in Fig. 1, assuming properties of the ICM typical of massive clusters. The relativistic corrections for a range of ICM temperatures are also shown, which highlights the temperature dependence of the rSZ corrections. Since the classical (non-relativistic) tSZ brightness is sensitive solely to the product $n_e T_e$ at a given x , it alone cannot be used to isolate the electron temperature. However, the spectrum of the relativistic correction depends on T_e , and thus offers a way to probe electron temperature independent of X-ray observations (Remazeilles 2022).

The rSZ is an emerging observable tool that can be used to independently assess the extremely high gas

temperatures present in some media, with the shock-heated ICM being an example. The typical small change in SZe amplitude induced by the correction and its spectral degeneracy with the tSZe and kSZe below 300 GHz has restricted its use in traditional radio- and mm-wavelength observations. However, combining sensitive mm-wavelength measurements with sub-mm measurements has been demonstrated to be a potentially fruitful way to isolate the rSZe corrections and explore extreme ICM temperatures (Zemcov et al. 2010, 2012; Butler et al. 2022), and recent statistical measurements using *Planck* have also utilized the rSZe as a probe of ICM temperature (Hurier & Tchernin 2017; Erler et al. 2018; Remazeilles & Chluba 2025).

In this work, we describe an analysis wherein observations from the *Herschel* Space Observatory’s Spectral and Photometric Imaging REceiver Fourier Transform Spectrometer (SPIRE-FTS; Naylor et al. 2014) are used to constrain the rSZe signal from the quadruple-merger MACS J0717.5+3745 (Ma et al. 2009; Sayers et al. 2013; Adam et al. 2017; Breuer et al. 2024). Between 500–900 GHz the fractional contribution of the rSZe correction is maximized (Fig. 1), and its spectral behavior removes degeneracies with the classical T_{SZe} distortion. These measurements of the SZe spectra with a resolving power $\lambda/\Delta\lambda = R \simeq 30$ from a fully spectrometric instrument provide a space to explore feasibility, assess the effects of various systematic errors, and provide new insights on the state of the cluster’s ICM.

This paper is organized as follows. In Section 2 we describe the primary and ancillary data used in our analysis and how instrument systematics are removed from the data. Section 3 is a detailed presentation of the SPIRE-FTS data reduction. In Section 4 we describe the fitting procedure and in section 5 we discuss our results in the context of past and future rSZe measurements.

2. DATA

To measure the rSZe in MACS J0717.5+3745, we combine observations from the SPIRE-FTS (Griffin et al. 2010) with a variety of ancillary observations at a wide range of wavelengths. Following reduction of the SPIRE-FTS measurements to data hypercubes, they are combined with Bolocam (Glenn et al. 2003) intensity measurements to determine the spectrum of the SZe (§4). Next, *Herschel*-SPIRE photometer observations are used to estimate the contaminating signal contributed by dusty infrared galaxies, and cluster member velocity maps are used as a prior on the ICM velocity (Silich et al. 2024). The corrected intensity spectra are then modeled and various ICM and instrumental param-

eters are constrained, including T_{rSZe} . Finally, the X-ray derived temperatures are combined in a way that makes them comparable to the rSZe measurements. Maps summarizing the data sets are shown in Figure 2, and a compilation of fiducial values from each of the data products listed above at each position shown in Figure 2 are provided in Table 2. In the following section we present a summary of each source of data.

2.1. The *Herschel* SPIRE-FTS

The SPIRE-FTS instrument employed a Mach-Zehnder interferometer (Naylor et al. 2003) as a Fourier transform spectrometer (FTS) with two input ports. The first FTS input was illuminated by the *Herschel* telescope, while the second FTS input port was coupled to the Spectrometer Calibrator (SCAL), a cryogenic temperature-controlled source designed to load-match emission from the *Herschel* primary optics (Dohlen et al. 2000). The SPIRE instrument team found that SCAL was not necessary to compensate for the telescope emission during routine observations, but it noticeably increased the photon noise when heated (Swinyard et al. 2010). As a result, SCAL was left to drift with the temperature of the optical bench around 4.5 K, and for most SPIRE-FTS observations did not play a role. Here we treat the SPIRE-FTS as a low-resolution spectrophotometer sensitive to continuum emission, therefore the SCAL emission will induce a systematic in our data, as discussed further in Section 3.1.

The SPIRE-FTS output focal plane was populated by independent bolometer arrays coupled to the FTS element via a dichroic beamsplitter. The long wavelength array (termed “SLW”) covered 447–1018 GHz and comprised 19 detectors in a hexagonal close-packed pattern, as described in Griffin et al. (2010). There are known difficulties connecting the continuum brightness measured in the short wavelength array to SLW (Valtchanov et al. 2018), and since the high frequency data does not constrain the SZe emission in a useful way we opted to ignore them in this study.

An internal beam steering mirror near the input of the spectrometer permitted spatial modulation of the telescope beam and is used to “jiggle” the field of view of the focal plane array to produce fully-sampled images. The observations under study were performed in the intermediate sampling mode of the instrument, which comprises four jiggle positions separated by one beam-width (Benielli et al. 2014). The change in optical configuration was also the source of a strong instrumental systematic, as discussed in Section 3.1.

The fundamental SPIRE-FTS data product is an interferogram acquired over an FTS scan with temporal

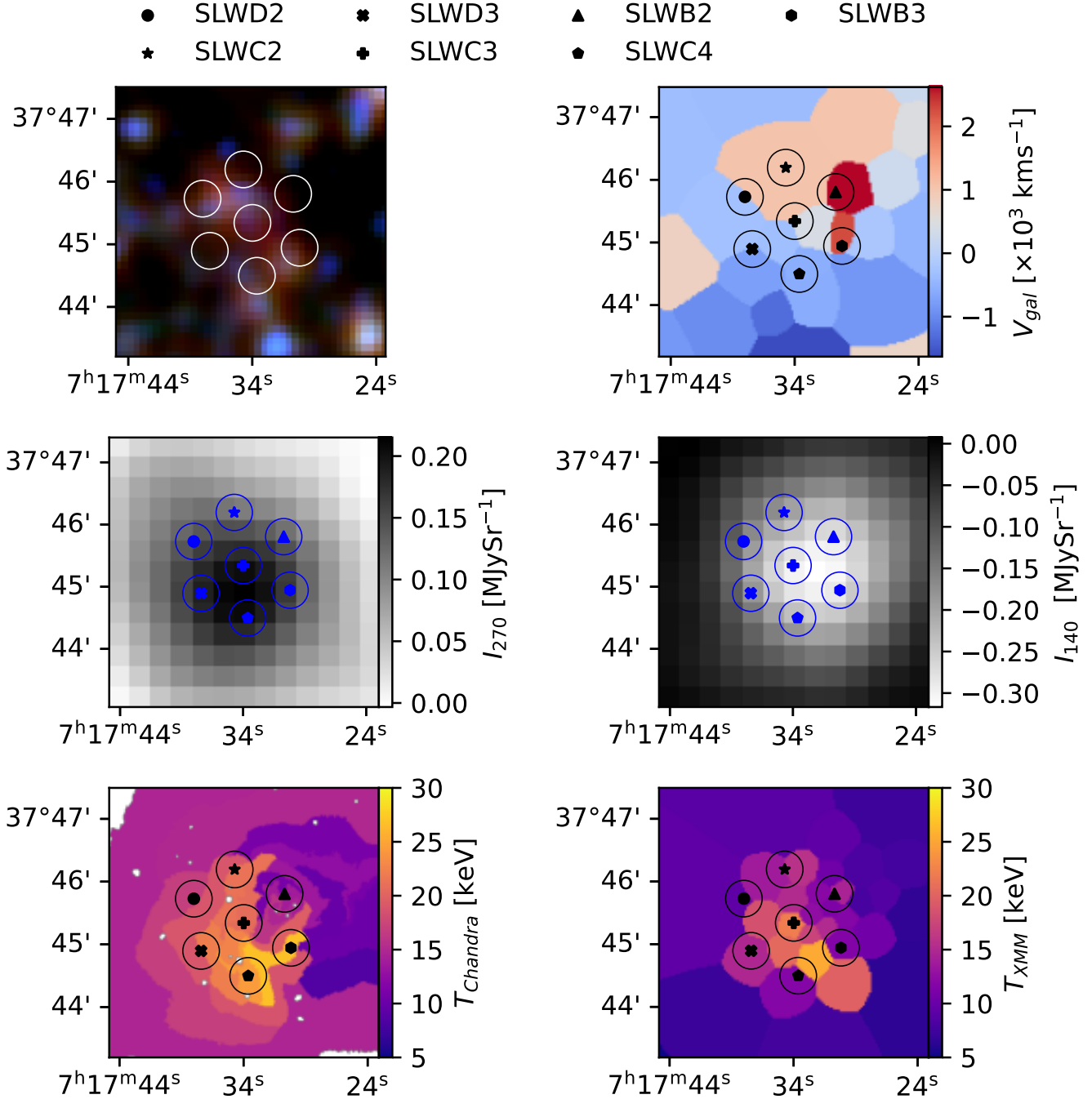


Figure 2. Datasets used in this analysis. The markers (labeled at the top) and circles show the average pointing location and effective beam size for each SPIRE-FTS SLW detector considered in this work. Top left: false color image of MACS J0717.5+3745 from the *Herschel*-SPIRE photometer where red represents 600 GHz emission, green 856 GHz, and blue 1200 GHz. Top right: velocity map from cluster-member redshifts. Middle row: Bolocam measurements of the SZE intensity at 270 and 140 GHz. Bottom row: electron temperature measured by *Chandra* and *XMM-Newton*.

duration set by the desired spectral resolving power. The interferograms are processed through the *Herschel* Interactive Processing Environment (HIPE; Ott 2010; Fulton et al. 2016). Our observations (shown in Table 1) are taken in intermediate spatial sampling, $R \sim 30$

“low resolution” (LR) spectral mode. Four hundred interferograms were recorded per jiggle position per observation.

The standard SPIRE-FTS observation set included an observation of a “Dark Sky” field (Pearson et al. 2025)

Observation ID	Spec. Resolution	Spat. Resolution	Target Name	# of Scans	Date	Integration Time
1342252295	LR	I	MACS J0717.5+3745	400	2012 Oct 6	12139 s
1342252296	LR	I	MACS J0717.5+3745	400	2012 Oct 6	12139 s
1342252297	LR	SP	Dark Sky	400	2012 Oct 6	3192 s
1342252903	LR	I	MACS J0717.5+3745	400	2012 Oct 7	12139 s
1342252904	LR	I	MACS J0717.5+3745	400	2012 Oct 7	12139 s

Table 1. SPIRE-FTS observations used in this analysis listed in chronological order by observation date. Intermediate (I) spatial sampling refers to observations with 4 “jiggle” positions and single pointing (SP) to one jiggle position within an observation. The number of scans refers to the number of scans taken at a single jiggle position not the total number of scans across the entire observation.

near the north ecliptic pole used to monitor the characteristics of the instrument using a consistent, faint astrophysical background illumination (Hopwood et al. 2015; Marchili et al. 2017). All SPIRE-FTS observations have a companion Dark Sky observation taken in the same observing mode. However, the companion Dark Sky observation for the MACS J0717.5+3745 observations presented here has only one jiggle position, meaning there is no analogue Dark Sky measurement for three of the four optical configurations. We describe the impacts of this discrepancy in Section 3.1.

2.2. Bolocam

Bolocam was used to observe MACS J0717.5+3745 in two different photometric bands centered on approximately 140 and 270 GHz. The data (Planck Team 2015) are reduced to surface brightness maps using the methods described in Sayers et al. (2013) and Sayers et al. (2019). Here we make use of these surface brightness images in both bands, which both readily cover the field of view of the SPIRE-FTS at approximately uniform depth. The Bolocam map uncertainty is assumed to follow a Gaussian distribution with a standard deviation estimated from extracting the surface brightness from identical locations in 1,000 random noise realizations of the data. The FWHM of the Bolocam PSF, equal to $59''$ at 140 GHz and $33''$ at 270 GHz, is comparable to that of the SPIRE-FTS over the frequency range considered in our analysis. Therefore, we do not attempt to correct for any PSF effects in our surface brightness measurements. The precise values of I_{270} and I_{140} used throughout this work are shown in Table 2.

2.3. Cluster Member Redshifts

In the Bolocam bands, the kSZ signal due to the line-of-sight velocity of the gas can produce a non-negligible signal compared to the rSZ signal we aim to measure, as shown in Figure 1. Due to strong degeneracies between the amplitudes of the kSZ and tSZ signals, along with the gas temperature (which specifies the relativistic corrections to those signals), it is not possible to ob-

tain meaningful constraints on all three parameters with the existing spectral coverage. As demonstrated in Sayers et al. (2013) the line-of-sight gas velocities are consistent with the bulk dark matter velocities estimated from spectroscopy of cluster-member galaxies (Ma et al. 2009). We therefore use external data to place a prior on the gas velocity in the region of the cluster observed by the SPIRE-FTS.

Following the technique of Silich et al. (2024), we obtain a map of the dark matter velocity by spatially binning the cluster-member galaxy spectra. To summarize the analysis, we first define a spatial aperture based on the cluster-member galaxy distribution by convolving a cluster-member galaxy count map constructed via the redshift catalog of Ma et al. (2009) with a $2'$ peak-normalized top-hat kernel. This new map is then smoothed via convolution with a $3'$ FWHM area-normalized Gaussian kernel. We then draw a contour within which each pixel has $\gtrsim 5$ galaxies. To close the contour at large radii, we define a circular aperture with $r = 6.5'$ ($\simeq 2.5$ Mpc at $z \simeq 0.5$). At any point where the drawn contour would remain open at this circular boundary, we close the contour with the circular aperture. Within this aperture, we generate the spatial bins for the cluster-member galaxy velocity map by applying a publicly-available Python implementation of the weighted Voronoi tessellation algorithm (Diehl & Statler 2006; Rhea et al. 2020) to our galaxy counts map, requiring 10 galaxies per spatial bin to ensure statistical significance and consistency between pixels. We then apply an estimator from Beers et al. (1990) to populate the cluster-member galaxy velocity in each bin.

2.4. X-ray Spectroscopy

We derive X-ray inferred gas temperatures from both *Chandra* and *XMM-Newton* to compare with our derived values of T_{rSZe} following the data processing techniques described below.

2.4.1. Chandra

Detector	SLWD2	SLWC2	SLWD3	SLWC3	SLWB2	SLWC4	SLWB3
v_{pec} [km s ⁻¹]	260 ⁺¹⁹⁰ ₋₁₉₀	930 ⁺³⁰⁰ ₋₃₀₀	-410 ⁺¹¹⁰ ₋₁₁₀	370 ⁺¹⁵⁰ ₋₁₅₀	1500 ⁺¹⁸⁰ ₋₁₈₀	-540 ⁺⁹⁰ ₋₉₀	250 ⁺¹¹⁰ ₋₁₁₀
T_{XMM} [keV]	12.3 ^{+0.4} _{-0.4}	12.8 ^{+0.4} _{-0.4}	14.1 ^{+0.5} _{-0.5}	16.9 ^{+0.4} _{-0.4}	11.7 ^{+0.2} _{-0.2}	15.7 ^{+0.5} _{-0.5}	14.3 ^{+0.4} _{-0.4}
T_{Chandra} [keV]	17.6 ^{+0.8} _{-0.8}	17.0 ^{+0.7} _{-0.7}	19.6 ^{+0.8} _{-0.8}	19.7 ^{+0.6} _{-0.6}	14.2 ^{+0.3} _{-0.3}	21.7 ^{+0.9} _{-0.9}	17.2 ^{+0.7} _{-0.7}
I_{140} [MJy sr ⁻¹]	-0.16 ^{+0.02} _{-0.02}	-0.20 ^{+0.02} _{-0.02}	-0.18 ^{+0.02} _{-0.02}	-0.31 ^{+0.02} _{-0.02}	-0.29 ^{+0.02} _{-0.02}	-0.23 ^{+0.02} _{-0.02}	-0.30 ^{+0.02} _{-0.02}
I_{270} [MJy sr ⁻¹]	0.15 ^{+0.02} _{-0.02}	0.12 ^{+0.02} _{-0.02}	0.18 ^{+0.02} _{-0.02}	0.21 ^{+0.02} _{-0.02}	0.13 ^{+0.02} _{-0.02}	0.20 ^{+0.02} _{-0.02}	0.16 ^{+0.02} _{-0.02}
R.A.	07 ^h 17 ^m 38 ^s 01	7 ^h 17 ^m 34 ^s 72	7 ^h 17 ^m 37 ^s 43	7 ^h 17 ^m 33 ^s 99	7 ^h 17 ^m 30 ^s 70	7 ^h 17 ^m 33 ^s 63	7 ^h 17 ^m 30 ^s 18
Decl.	37° 45′ 43″.7	37° 46′ 11″.68	37° 44′ 53″.77	37° 45′ 20″.52	37° 45′ 48″.36	37° 44′ 29″.91	37° 44′ 56″.7

Table 2. Parameter values obtained from the auxiliary data for each of the seven SPIRE-FTS pointing positions shown in Figure 2. The prior on ICM velocity utilized in our fits, v_{pec} is derived from data in Section 2.3 and described in Section 4. Electron temperatures from XMM-Newton and Chandra are derived from the data described in Sections 2.4.1 and 2.4.2 using the algorithm presented in Section §2.5. The 140 and 270 GHz intensities were obtained from Bolocam as detailed in Section 2.2.

The reduction and analysis of the Chandra data are described in detail by Mantz et. al (in preparation), using CIAO version 4.16 and CALDB version 4.11.0. In brief, the archival data (Observation 1655, CXC-DS (2002)) were reprocessed using standard techniques to produce level 2 event files, and filtered to remove periods of enhanced background. The source detection code WAVDETECT was used to find point-like sources, which were masked in later analysis. Images were produced in the 0.6–7.0 keV band, binned to 0.984″ resolution, and regions for spectral analysis were defined using the CONTBIN algorithm (Sanders 2016) with a target signal-to-noise of 55 and a geometric constraint parameter of 2. Spectra in these regions were modeled as the sum of a Galactic soft foreground, constrained by ROSAT All-Sky Survey data (Sabol & Snowden 2019); emission from active galactic nuclei fainter than the WAVDETECT detection limit; the quiescent particle-induced background (Suzuki et al. 2021); and absorbed thermal emission from the ICM, using the APEC code and adopting an equivalent absorbing hydrogen column density of $N_H = 6.92 \times 10^{20} \text{ cm}^{-2}$ (HI4PI Collaboration et al. 2016). Full details of the foreground and background modeling, including systematic allowances marginalized over can be found in Mantz et. al (in preparation). All spectra were fit in the 0.6–7.0 keV observer-frame band using XSPEC (version 12.12.1c) to evaluate the likelihood and the LMC python package to sample the posterior distribution. The analysis assumed a common ICM metallicity among all regions, allowing the temperatures and normalizations to fit independently. The resulting map of best-fitting temperatures is shown in Figure 2.

2.4.2. XMM-Newton

We use the European Photon Imaging Camera (EPIC) to observe this cluster with XMM-Newton. This instrument uses two types of cameras; pn CCDs and MOS CCDs. We use observation 0672420201, and the data

files were reprocessed using the XMM-Newton Science Analysis System v19.1.0. We employed the tasks *emchain* and *epchain* to generate calibrated event files from the raw data. For the pn camera, an out-of-time (OOT) event file was also produced using *epchain*. To ensure data quality, we excluded all events with PATTERN>12 for the MOS cameras and PATTERN>4 for the pn camera. Additionally, events adjacent to CCD edges and those associated with bad pixels were removed by applying FLAG = 0 for all cameras. We also excluded data from CCDs identified as being in an anomalous state, following the criteria described by Kuntz & Snowden (2008). Finally, periods of high background were filtered out using the *mos-filter* and *pn-filter* tasks.

Spectral analysis was carried out using the XSPEC package (Arnaud 1996), version 12.12.0. The energy ranges considered were 0.5–12 keV for the MOS cameras and 0.5–14 keV for the pn camera. The X-ray emission was modeled with an APEC thermal plasma model (Smith et al. 2001), adopting elemental abundances from Asplund et al. (2009) and employing C-statistics for the spectral fitting.

Photoelectric absorption was fixed to the total hydrogen column density including both neutral and molecular components using the value $N_H=8.36 \times 10^{20} \text{ cm}^{-2}$, as reported by Willingale et al. (2013). The MOS and pn spectra were fit simultaneously, with the temperature and metallicity parameters linked across instruments while allowing the normalizations to vary independently. The XMM-Newton background modeling is rather complicated and we defer the interested reader to Lovisari & Reiprich (2019) for a detailed description.

The temperature map shown in Figure 2 was produced following the methodology described in Lovisari et al. (2024). Spatial regions were defined using the WVT binning algorithm (Diehl & Statler 2006), a generalization of the Voronoi binning technique introduced by Cappell

lari & Copin (2003), with a signal-to-noise requirement of $S/N \geq 50$.

2.5. Extracting Fiducial Values from Tessellated Maps

The maps of cluster member galaxy velocities and the electron temperatures from both *Chandra* and XMM-*Newton* are composed of irregular-shaped regions defined by the WVT or `contbin` procedures. To extract the fiducial values of the velocity fields at each of the SPIRE-FTS pointings we use a PSF-weighted average computed from the entire map. The weighting factor is given by $\frac{B}{\sigma^2}$ where B is the fraction of the PSF that couples to a given region and σ is the measurement uncertainty on the quantity within that region. The SPIRE-FTS SLW bands’ PSF depends on frequency channel, but we make the approximation that it has a Gaussian shape with a FWHM equal to $35''$ for all channels. Conversely, for the temperature maps we opt to use a per-pixel bin weighting because of the fact that the X-ray `contbins` are chosen to have an approximately equal number of total counts and thus an inverse variance weighted approach would be biased towards lower temperatures. The extracted temperature values and their uncertainties are estimated via a Monte Carlo sampler. We produce 10^4 realizations of the temperature maps where each spatial bin is varied as a Gaussian-distributed draw with mean and standard deviation set by the central value and measurement uncertainty. The fiducial temperatures are then taken to be the median and standard deviation of this set of 10^4 realizations and are shown, alongside the fiducial velocity values, in Table 2.

3. SPIRE-FTS DATA REDUCTION

To produce sub-mm spectra that can be compared against models for the rSZe, the raw interferograms reported by the SPIRE-FTS are corrected for detector and optical effects, calibrated, and mapped onto spectral cubes. Systematic instrumental effects are then modeled and removed. The resulting spectral hypercubes are then corrected for foreground astrophysical emission to produce estimates of the diffuse SZe signal.

3.1. Spectral Intensity Estimation and Data Cuts

The HIPE Spectrometer Mapping User Reprocessing Script v.14 is used to generate a spectrum of MACS J0717.5+3745 at each of the 112 pointing positions (7 detectors \times 4 observations \times 4 jiggle positions) using the v14.3 SPIRE-FTS calibration tree. A threshold of 4 is used for the baseline correction, and Level 2 deglitching is performed with the MAD algorithm. The `spectrum2d` object is made with beam diameters estimated from SLWC3 and the extended source calibration

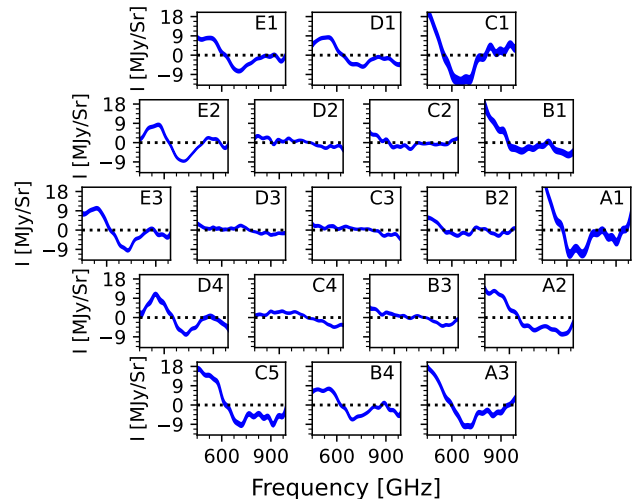


Figure 3. The Dark Sky observation described in Table 1 as processed through HIPE following the procedure outlined in §3.1 including the standard LR correction. The widths of the lines represent the per-datum error estimate from HIPE. A systematic pattern associated with beam vignetting is evident in the outer ring of detectors; for example, the average standard deviation of the intensity of these outer ring detectors is 6.3 MJy sr^{-1} compared to 1.9 MJy sr^{-1} for the inner detectors. There remains a low frequency increase up to $\sim 6 \text{ MJy sr}^{-1}$ that is consistent with a 4.5 K blackbody, as we would expect from the beam intercepting cold optics with slowly varying temperatures.

correction is applied. In Figure 3 we present calibrated spectra produced using the HIPE pipeline with the parameters described above, including the standard LR-mode correction. Notably, the deviation of the outer ring detectors is about $3\text{--}4\times$ that for the central detectors, and exhibits strongly correlated low-frequency variation over the passband. This is due to a known vignetting effect in the instrument (Benielli et al. 2014) that we find is too severe to model adequately. We therefore opt to perform our analysis on only the seven central detectors where the vignetting is not present and the SZe signal is largest.

An LR-mode correction implemented as an empirical model (Marchili et al. 2017) is normally used to correct an aliased instrumental signal in HIPE. The signal itself appears as a “double bump” in the continuum that we refer to as the Marchili signal. The spectra in Fig. 3 exhibit residual Marchili-like structure after processing through the standard HIPE pipeline, which we identify as arising from the generalized empirical approach developed in Marchili et al. (2017) not sufficiently subtracting the effect seen in the observed data. To improve the modeling of systematics, we turn off the standard LR-mode correction step in HIPE and instead use the Dark

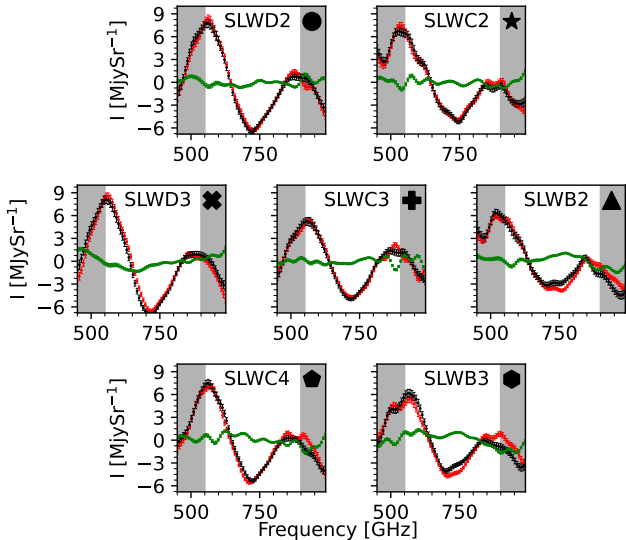


Figure 4. The signal after HIPE processing for each of the seven inner SLW bolometers. The black points denote the SPIRE-FTS spectrum that we retrieve from HIPE, the red points indicate the same for the Dark Sky observations, and the green points indicate the cleaned spectrum obtained from subtracting a scaled version of the Dark Sky data. We estimate the noise covariance of these cleaned data from Equation 5, and the square root of the diagonal elements are shown as error bars.

Sky observation to create a template for subtraction. This is motivated by the fact that the astrophysical signal in the Dark Sky observations is small, and that they are taken in the same observing mode and during identical thermal periods as each of our four observations. They are thus a reliable tracer of the instrumental systematics in a time-adjacent sense, and provide a better template for subtracting the aliased Marchili signal.

The process for creating the Dark Sky templates from each detector spectrum proceeds as follows. For each detector i and pointing position j , an amplitude scaling is computed according to $A_{ij} = \frac{\vec{s}_{ij} \cdot \vec{d}_i}{\vec{d}_i \cdot \vec{d}_i}$. The corrected spectrum is then computed from $\vec{s}_{c,ij} = \vec{s}_{ij} - A_{ij} \vec{d}_i$. The \vec{s} , $A \vec{d}$ and \vec{s}_c for each detector are shown in Figure 4. For the jiggle position 0 data, this template subtraction leaves a residual with a standard deviation of 0.6 MJySr^{-1} , approximately a factor of three better than what was achieved using the standard correction and with no discernible Marchili-like structure. However, this correction works less well for the three jiggle positions that were not present in the Dark Sky observation, which constitute different optical paths through the instrument, and leaves residual Marchili-like structure due to incomplete cancellation. We therefore opt to exclude data taken in jiggle positions $\{1, 2, 3\}$ from

analysis, which increases the statistical uncertainty by a factor of two but removes a likely uncharacteristic systematic error from the measurement.

Figure 4 illustrates a remaining mismatch between the data and Dark Sky template at frequencies near the band edges, again likely arising from instrumental systematics. To produce a calculable figure of merit to inform which spectral information to exclude, we estimate the per spectral channel constraining power as follows. We model the rSZe spectrum using fiducial values from Bolocam measurements and with varying temperature. The constraining power on T_{rSZe} is then calculated from:

$$\sigma_T^2 = \left(\frac{\sigma_I}{\delta I_T} \right)^2. \quad (3)$$

Here σ_I is the per spectral channel uncertainty and δI_T is the partial derivative with respect to T_{rSZe} . The inverse-squared of this is plotted as a function of spectral channel, and for several different values of T_{rSZe} , in Figure 5. We conclude the optimal spectral region is 550–900 GHz, as the sensitivity to the rSZe signal outside of this range is small and including those data would significantly increase the measurement error. This range also removes the portions of the spectra that may contain significant instrumental systematics.

3.2. Spectral Noise Estimation

A covariance matrix is estimated using a time-wise jackknife resampling that is designed to cancel spatially and spectrally stable signals in our data, e.g from astrophysical sources or instrument thermal emission, while retaining variations due to statistical noise and properties of the instrument varying on the scan time scale. To generate this estimate, two hundred of the four hundred spectra for a given pointing are multiplied by negative 1, and the mean is computed with:

$$\vec{s}_l^* = \frac{\sum_k \vec{s}_{k\pm}}{2N_{scan}}. \quad (4)$$

Here $\vec{s}_{k\pm}^*$ denotes the sum over all four hundred spectra for a given pointing where indices with a minus sign are multiplied by negative one and indices with a plus sign are kept the same. The resulting covariance matrix is estimated by computing the outer product of \vec{s}_l with itself,

$$C_l = \vec{s}_l^* \vec{s}_l^{\text{T}} \quad (5)$$

where T denotes the matrix transpose. This process is repeated 2×10^6 times (chosen to estimate the covariance matrices to five significant figures) and averaged. We perform these jackknives independently for each detector, jiggle position (only jiggle position 0 is used in the

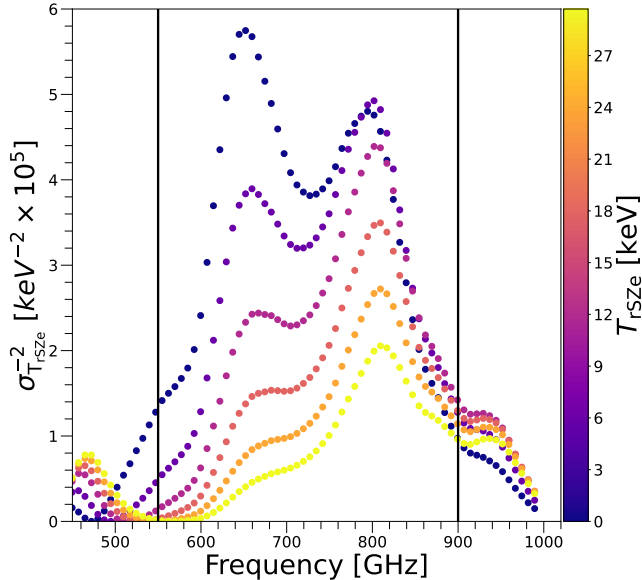


Figure 5. The constraining power on T_{rsze} estimated by the inverse square of equation 3. The solid black vertical lines highlight where the low and high frequency cuts from §3.1 are applied, and outside of which the constraining power is small. While the SZe distortion is spectrally smooth (see Fig. 1), the relativistic corrections exhibit ~ 100 GHz-wide spectral deviations whose relative amplitudes change over the falling edge of the SZ spectrum. These differential effects provide a lever arm to distinguish gas at different temperatures independently of X-ray information. Hence, the constraining power peaks at 640 and 800 GHz. This is informative for cutting the low and high frequency ends of the FTS bandpass, as the regions with very low constraining power, e.g. $\nu < 550$, will contribute disproportionately more noise to the measurement.

analysis), and observation, producing 28 unique covariance matrices. Since we expect multiple observations with the same detector to have consistent systematics we average these by detector down to a total of seven. A representative example showing the correlation matrix, which is estimated from the noise covariance matrix, is shown in Figure 6. The characteristic correlation length implied by the noise covariance is approximately 50 GHz, comparable to the nominal LR spectral resolving power of 25 GHz.

3.3. Unwanted Astrophysical Emission

The largest source of astrophysical emission towards MACS J0717.5+3745 is from the dusty infrared galaxies that make up the cosmic infrared background (CIB). The thermal dust emission from these galaxies peaks near $100 \mu\text{m}$ and is redshifted to fall in the *Herschel*-SPIRE bandpass (Planck Collaboration et al. 2011). The CIB signal is much bluer than the SZe signal (Erler et al. 2018; Planck Collaboration et al. 2016; Butler et al.

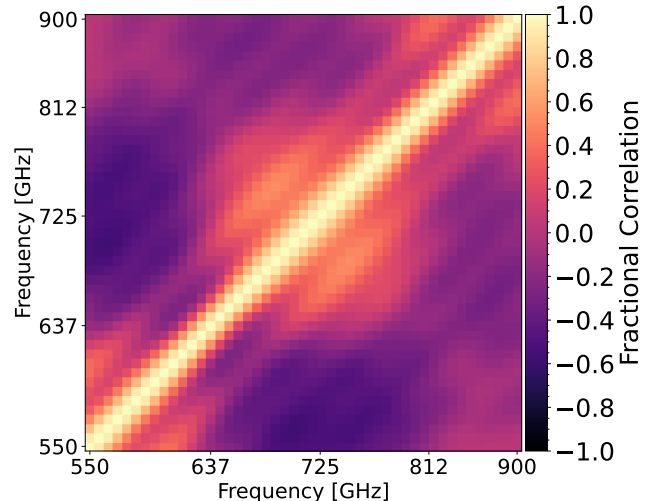


Figure 6. A representative noise correlation matrix for a single SPIRE-FTS detector. This is computed from the noise covariance matrix C defined in eq 5, as $D^{-1}CD^{-1}$, where D is a matrix containing only the square root of the diagonal elements of C . The effective correlation length is of order 50 GHz.

2022), and is brightest where the SZe intensity is negligible above 1 THz. As a result, it is possible to estimate the contribution of the CIB to the SPIRE-FTS observations using *Herschel*-SPIRE photometer data. We compute a model for the CIB galaxy emission in the cluster in three steps. First, we use the Probabilistic Cataloging in the Presence of Diffuse Emission (PCAT-DE; Feder et al. 2023) software to measure the flux densities and positions of point-like sources coincident with the galaxy cluster using data from the three *Herschel*-SPIRE photometer bands (§3.3.1). Next, we fit a greybody spectrum to the spectral energy distribution (SED) of each recovered source (§3.3.2). Lastly, we create mock CIB maps at each SPIRE-FTS frequency to infer the contribution of the CIB to the FTS Observations (§3.3.2) and subtract this model from the spectral data. Each of these steps is described below.

3.3.1. Source Catalog Generation

PCAT-DE uses a Bayesian hierarchical model to jointly fit the flux density and position of point-like sources, the fluctuation and amplitude of diffuse foreground/background components, and the amplitude of surface brightness templates over a set of multi-band photometric maps (Feder et al. 2023). In this analysis, we use PCAT-DE to recover the point source SEDs from the *Herschel*-SPIRE photometer maps of MACS J0717.5+3745.

To construct a point source catalog, MACS J0717.5+3745 photometer images in all three

Herschel-SPIRE bands (600, 856, and 1200 GHz) are modeled using a modified version of the procedure developed for [Butler et al. \(2022\)](#). Because our goal is to recover a model of the sources comprising the CIB, we fix the SZe template amplitudes for the PMW and PLW bands to their fiducial values from Bolocam measurements of the optical depth ([Sayers et al. 2019](#)) and the X-ray inferred temperature from *XMM-Newton* (§2.4) so that the SZe is no longer a free parameter. Point sources, the cirrus foreground, and an overall offset are then fit over a $10' \times 10'$ region centered on the X-ray centroid of the cluster, as described in [Feder et al. \(2023\)](#). This results in a PCAT source catalog describing the positions and fluxes of point sources that is decoupled from diffuse sources of emission in the cluster field.

Residuals between the input *Herschel*-SPIRE photometer maps and the CIB point source model constructed by *PCAT* are shown in Figure 7. The CIB model removes point source emission from all three bands and leaves a strong diffuse signal that is brightest in the 600 GHz band, consistent with the SZe. A false three-color image of the residuals that can be directly compared to the upper left panel of Figure 2 is also shown in Fig. 7. This visually illustrates our high-SNR measurement of diffuse SZe emission in MACS J0717.5+3745 with the *Herschel*-SPIRE photometer.

3.3.2. CIB Correction

With a reliable point source catalog, we can next model the spectrum of each point source. A greybody spectrum (e.g., [Planck Collaboration et al. 2014](#)) is fit to the SED of each photometer source identified by PCAT,

$$I_\nu = \frac{\epsilon}{B(\nu_p, T_{dust})} B(\nu, T_{dust}) \left(\frac{\nu}{\nu_p} \right)^\beta, \quad (6)$$

where the free parameter ϵ describes the amplitude of the source in mJy and T_{dust} the temperature of the dust. We set the pivot frequency at $\nu_p = 856$ GHz and fix $\beta = 1.65$ to match the *Planck* model ([Planck Collaboration et al. 2016](#)). The fits are implemented via a Monte Carlo markov chain (MCMC) sampler ([Foreman-Mackey et al. 2013](#)) with loss function given by the χ^2 distribution. Uniform priors of $T_{dust} \in [5, 200]$ K and $\epsilon \in [0, 10^5]$ mJy ensure that these fits remain within a physically meaningful space of values. The fit outputs are posterior distributions for ϵ and T for each of the PCAT-detected sources in the cluster region. On a source-by-source basis SEDs from these posterior predictive distributions are sampled in the SPIRE-FTS spectral binning, which allows us to create a probability distribution of flux densities for each source $\{F_{\nu,s}\}$.

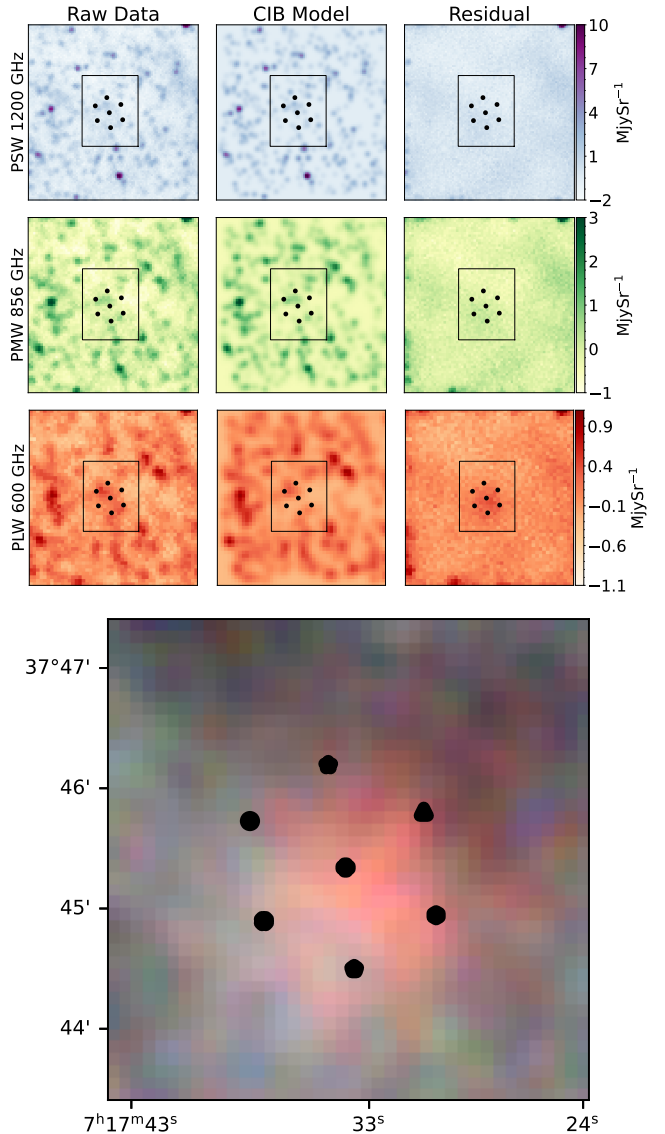


Figure 7. *Herschel*-SPIRE photometric imaging of MACS J0717.5+3745. From top to bottom the rows show PSW (1200 GHz), PMW (856 GHz), and PLW (600 GHz). From left to right the columns show the observed image centered on MACS J0717.5+3745, a fitted CIB point source model constructed using PCAT-DE ([Feder et al. 2020](#)), and the residual after subtraction of this model. The pointing of each of the seven detectors are shown as black dots. This demonstrates that we are able to accurately remove CIB contamination while preserving the SZe signal, as primarily seen in the 600 GHz panel. The bottom panel is a false color image of the three residuals illustrating our high-SNR measurement of a diffuse signal consistent with the extremely red spectrum expected from the SZe.

From these probability densities, we generate mock catalogs and project them into corresponding mock images. We create a set of 5,000 such mock catalogs to

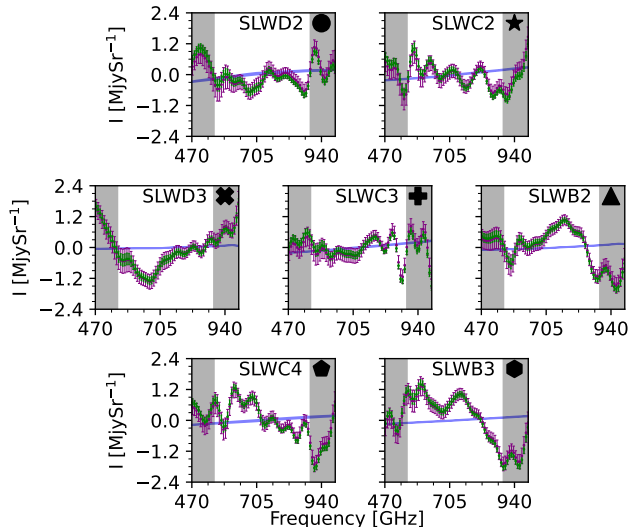


Figure 8. Residuals of the measured spectra and CIB model for each of the seven detectors used in this analysis. The purple points show the Dark Sky template-subtracted signal shown in Fig. 4, the blue curve is the estimated CIB spectrum with width set by the 68% model uncertainty, and the green points are the CIB-subtracted measurements. The CIB corrections act to preferentially reduce flux at high frequencies, as one would expect from the typical greybody model of a dusty infrared galaxy at this redshift.

better sample the source to source covariance derived from the PCAT catalog posterior. For each catalog, we assume that each source is point-like and convolve with the frequency dependent SPIRE-FTS PSF to obtain a mock map. Each source’s location is fixed to the median position obtained from PCAT-DE. We then extract the observed flux density in each of the 28 SPIRE-FTS pointing sets for jiggle position 0. The flux density from CIB sources is taken as the ensemble median over the set of 5,000 images in each pointing. These spectra are then averaged per detector, and the uncertainties of the averaged pointings are added in quadrature, the CIB estimates for each detector are shown in Figure 8. For each CIB model a diagonal covariance matrix is formed with diagonal elements given by the uncertainty estimated above. After subtraction of the CIB model, the final noise covariance matrix for these observations is formed from the sum of the noise covariance matrix estimated from the jackknives as described in Section 3.2 and the posterior variance of the CIB model.

4. SZE MODELING AND INFERENCE

We model the total SZe signal with

$$\Delta I = \Delta I_{kSZ_e}(\nu; y, v_{\text{pec}}, T_{\text{rSZ}_e}) + \Delta I_{tSZ_e}(\nu; y, T_{\text{rSZ}_e}) + O_{\text{FTS}}, \quad (7)$$

where v_{pec} is the peculiar velocity of the ICM, y is the total Comptonization parameter, and T_{rSZ_e} is the ICM temperature estimated by the rSZ_e, which is assumed to be constant along the line of sight. To marginalize over the absolute signal baseline of the SPIRE-FTS data, which is unconstrained, we include the term O_{FTS} that describes an additive offset to the sub-mm data. We jointly fit the CIB-corrected SPIRE-FTS spectra shown in Figure 8 and the Bolocam 140 and 270 GHz data (described in §2.2) to this model to constrain the free parameters. The nuisance parameter O_{FTS} is fit to the SPIRE-FTS data points only, and does not contain information of astrophysical importance. The data is fit with a MCMC sampler that evaluates ΔI_{kSZ_e} and ΔI_{tSZ_e} for each parameter combination using SZPACK (Chluba et al. 2012, 2013). As part of this fit, we include uniform priors on $T_{\text{rSZ}_e} \in [0, 60]$ keV and $y \in [0, 1]$. The lower bounds are designed to ensure the MCMC does not sample negative values, which are not physically allowed. The upper bounds are designed to be minimally informative, and do not noticeably impact the recovered posteriors. We also include an informative Gaussian prior on the value of v_{pec} based on the cluster-member redshifts derived in §2.3 and quantified in Table 2, as well as absolute bounds of $v_{\text{pec}} \text{ c}^{-1} \in [-0.1, 0.1]$.

The MCMC chains are initialized using random draws of the parameter values that sample the parameter space near the values of T_{rSZ_e} , v_{pec} and y predicted from the fiducial values in Table 2. The initial draws for the nuisance parameter O_{FTS} are $\in [-2.5, 2.5]$ MJySr⁻¹. We run each of these chains for twenty thousand steps, and we cut the first three thousand steps as the burn-in samples. A Gelman-Rubin statistic (Gelman & Rubin 1992) is used to assess the convergence of the chains, where we find that $\hat{R} = 1.0$ and only has variation across all detector fits at the level of 10×10^{-5} . The marginalized posterior distributions of these fits are shown in Figures 9 and 10, and the maximum a posteriori (MAP) parameter values for each SPIRE-FTS detector are listed in Table 3.

If we assume that the ICM is isothermal, then the temperature measurements from the seven SPIRE-FTS detector positions can be combined to obtain an inverse variance weighted mean of $T_{\text{rSZ}_e} = 14.2^{+2.4}_{-2.4}$ keV. However, the data strongly suggest that there are variations in ICM temperature over the cluster face. The fit quality of this isothermal model is relatively poor, as quantified by a reduced χ^2 of 1.5 and corresponding PTE of 0.06. To account for such variations, we can extend

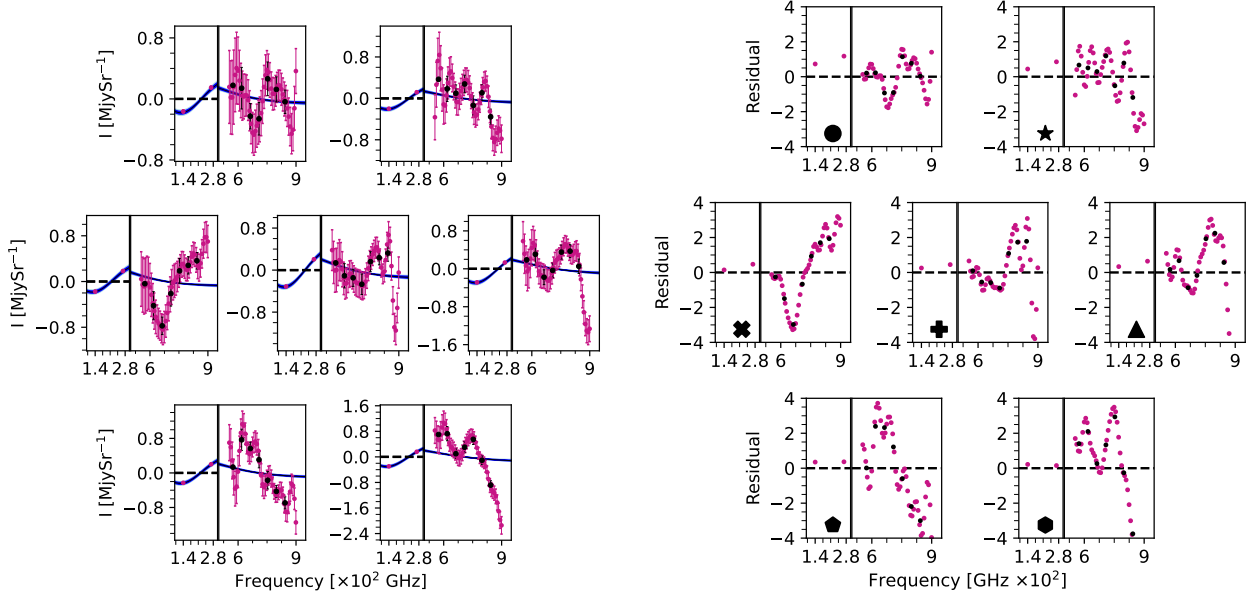


Figure 9. Best-fitting curves to the SZ spectrum from the combined SPIRE-FTS and Bolocam intensity measurements (pink points). The median fit is shown in black, with 1σ confidence intervals in blue and 2σ confidence intervals in light blue. The black data points show the SPIRE-FTS data averaged over a correlation length of six spectral channels. In the right hand panel we show the difference between the median fit and the data normalized by the uncertainty at each point.

Detector	SLWD2	SLWC2	SLWD3	SLWC3	SLWB2	SLWC4	SLWB3	Units
MAP T_{rSZe}	$9.5^{+7.3}_{-5.0}$	$21.4^{+11.1}_{-9.3}$	$8.2^{+4.8}_{-3.2}$	$14.5^{+7.8}_{-7.0}$	$25.6^{+10.6}_{-9.7}$	$15.2^{+5.8}_{-4.6}$	$29.5^{+8.0}_{-8.3}$	[keV]
MAP y	17.0^{+2}_{-2}	21.0^{+3}_{-3}	19.0^{+2}_{-2}	31.0^{+3}_{-3}	29.0^{+4}_{-3}	25.0^{+2}_{-2}	33.0^{+3}_{-3}	$[\times 10^5]$
MAP O_{FTS}	$-0.06^{+0.02}_{-0.02}$	$-0.1^{+0.03}_{-0.03}$	$-0.08^{+0.01}_{-0.02}$	$-0.17^{+0.03}_{-0.04}$	$-0.14^{+0.04}_{-0.03}$	$-0.11^{+0.02}_{-0.02}$	$-0.18^{+0.03}_{-0.03}$	[Mjy sr $^{-1}$]
MAP v_{pec}	140^{+180}_{-160}	840^{+280}_{-280}	-400^{+110}_{-110}	340^{+140}_{-140}	1470^{+170}_{-170}	-540^{+90}_{-90}	240^{+110}_{-110}	[km s $^{-1}$]

Table 3. Maximum a posteriori (MAP) values for the parameters of our fit to each of the seven SPIRE-FTS detectors. Error bars indicate 68 per cent credible regions.

the model to also include intrinsic scatter between the seven detector positions. We perform this fit with the *LRGS* python package (Mantz 2016), obtaining a mean temperature of $T_{rSZe} = 15.1^{+3.8}_{-3.3}$ keV with an intrinsic scatter of $\sigma_{rSZe} = 5.4^{+5.1}_{-3.4}$ keV.

To assess potential biases in our fitting procedure, we created 100 mock data sets of the rSZ data with realistic noise generated through a Cholesky decomposition. For each mock, the input value of T_{rSZe} is drawn from a Gaussian distribution with $\mu = 19.5$ keV and $\sigma = 12$ keV. The other parameters are drawn from the posterior distributions shown in Figure 10 and in Table 3. Each of these mocks is then to fit in the same manner as the SPIRE-FTS data, producing a set of 100 best fit temperatures. We re-sample these outputs with a jackknife method, wherein 10^4 sets of seven measurements are aggregated via the *LRGS* software package, following the same methodology as applied to the observed data. For each aggregate posterior we extract the MAP value and produce a set of 10^4 estimates. These

values are then compared to the mean temperature of 19.5 keV, and we find an on-average multiplicative bias of $1.016^{+0.003}_{-0.003}$. We conclude that the bias in T_{rSZe} from our fitting methodology is negligible compared to measurement uncertainties. Further, the recovered uncertainties on T_{rSZe} in the mock estimates are comparable to that of the recovered data.

5. DISCUSSION

Data from the SPIRE-FTS in combination with ground-based SZ data from Bolocam have permitted a high significance measurement of the ICM temperature in the quadruple merger MACS J0717.5+3745. We find a cluster-average temperature of $T_{rSZe} = 15.1^{+3.8}_{-3.3}$ keV with an intrinsic scatter over the cluster face corresponding to $\sigma_{rSZe} = 5.4^{+5.1}_{-3.4}$ keV. This work better establishes the rSZ as a viable tool for probing ICM thermodynamics, particularly of the extremely hot gas expected in major mergers (and confirmed in MACS J0717.5+3745 based on our analysis). In addi-

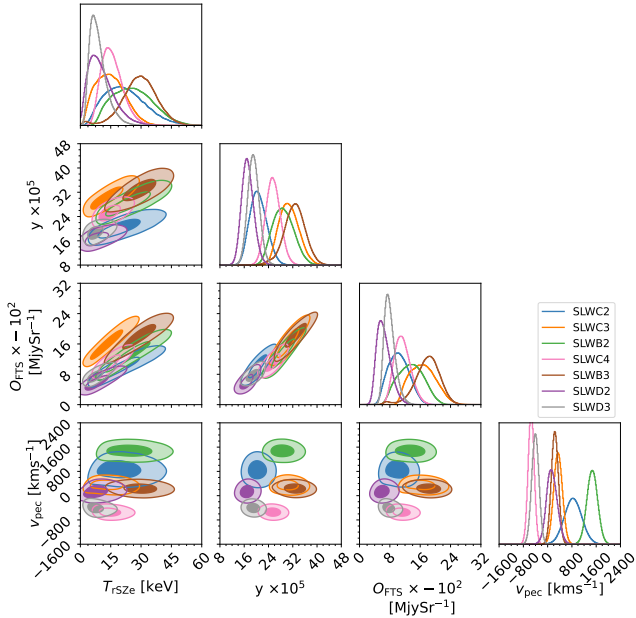


Figure 10. Posterior distributions for the fitted SZ parameters for each of the seven SPIRE-FTS detector positions. Fitted spectra corresponding to these parameter values are shown in Figure 9. The MAP values for each of the parameters being fit are shown in Table 3, and can be compared to the fiducial values shown in Table 2.

tion, while MACS J0717.5+3745 is a moderate redshift source, our analysis also serves to advance the rSZ as a potential path to probing the ICM in such systems at higher redshift.

It is informative to compare the ICM temperature we obtain from the rSZ against temperatures obtained from X-ray facilities. Differences between them may be expected from at least two sources. First, the differing line-of-sight weighting of the signals combined with non-isothermal distributions within the ICM can lead to discrepancies. Second, the presence of measurement systematics, in particular X-ray calibration uncertainties and band limitations, can also lead to different inferences about ICM temperature.

Regarding the first possibility, the rSZ measurement is effectively pressure-weighted so it is biased toward any gas in post-shock regions that has extreme temperatures and pressures (e.g., Mroczkowski et al. 2019). In contrast, the X-ray signal is biased toward high-density regions, which often correspond to low-temperature remnant cool cores in merging systems (e.g., Rossetti & Molendi 2010). In addition, differences are possible even in more quiescent systems, primarily as a result of cooling near the cluster center resulting in an enhanced gas density within that region (e.g., Hudson et al. 2010). As a consequence, the X-ray signal will be biased toward these cooler central regions, which would result in

a lower temperature compared to that derived from the rSZ.

Regarding the second possibility, we start by noting that there is a well established temperature calibration discrepancy between XMM-Newton and Chandra, which was studied in particular detail by Schellenberger et al. (2015), who established that at least one satellite has a large systematic error in its calibration. In general, they find that Chandra obtains higher temperatures than XMM-Newton, with a fractional difference of approximately 5–20 per cent for typical ICM temperatures, with larger fractional differences at higher temperatures. This difference provides a characteristic scale for the possible systematic error that may exist in their temperature measurements. While more difficult to quantify, we also reiterate the band limitations of the X-ray facilities noted in Section 1, which render them largely insensitive to photon energies $\gtrsim 8$ keV. Thus, both XMM-Newton and Chandra have little to no sensitivity to the hottest regions that may be present in the ICM, which could produce lower X-ray-derived temperatures for such regions.

To compute a characteristic X-ray temperature in a manner that best facilitates comparison to our rSZ-derived measurement, we determine the average temperature from the X-ray maps shown on the bottom row of Figure 2 at the same locations sampled by the SPIRE-FTS detectors, correcting for the PSF sampling according to the procedure described in Section 2.5. This yields a cluster-average temperature of $T_{\text{Chandra}} = 18.0^{+1.1}_{-1.1}$ keV from Chandra and $T_{\text{XMM}} = 13.9^{+0.9}_{-0.9}$ keV from XMM-Newton, shown as Fig. 11. While these values appear to be in mild tension, we note that the difference is almost exactly what is expected from the empirical relation derived by Schellenberger et al. (2015), and thus we attribute this tension solely to calibration uncertainties. The corresponding intrinsic scatters over the cluster face are $\sigma_{\text{Chandra}} = 2.8^{+1.3}_{-0.8}$ keV, and $\sigma_{\text{XMM}} = 2.2^{+1.0}_{-0.6}$ keV.

Combining the results of all three analyses, we find consistent average temperatures in the range of 15–20 keV for MACS J0717.5+3745. We firmly and independently establish that this major merger contains a significant amount of shock-heated gas from our rSZ analysis. In addition, other than the known calibration difference between XMM-Newton and Chandra, we find no evidence for differences in average temperature e.g. due to the specific distribution of gas density and temperature in MACS J0717.5+3745 or to potential biases from the band limitations of the X-ray facilities. While it may be tempting to utilize these measurements to better establish the temperature calibration of the

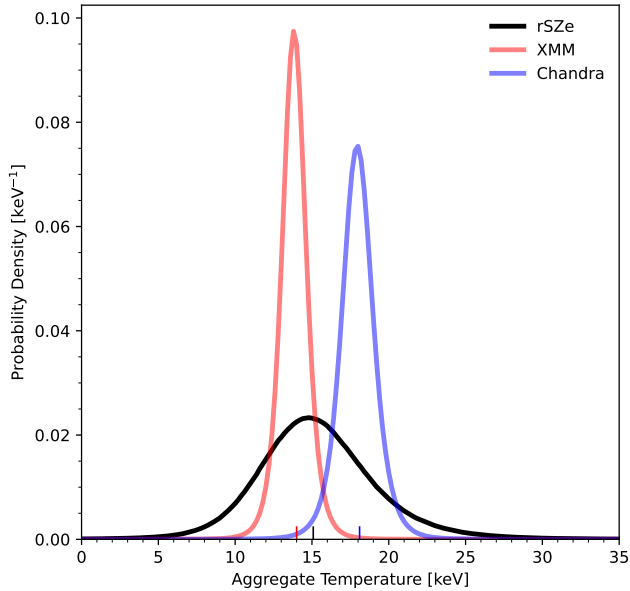


Figure 11. A comparison of the average temperatures obtained the rSZe and X-ray analyses. The posterior distribution of T_{rSZe} , accounting for detector-to-detector intrinsic scatter, is plotted in black, with $T_{\text{rSZe}} = 15.1_{-3.3}^{+3.8}$ keV. Applying the same procedure to the X-ray results yields $T_{\text{XMM}} = 13.9_{-0.9}^{+0.9}$ keV and $T_{\text{Chandra}} = 18.0_{-1.1}^{+1.1}$ keV.

X-ray satellites, we assert that such an inference is not justified due to the astrophysical and instrumental effects noted above, which are particularly relevant for an extremely hot merging system like MACS J0717.5+3745 even if they are not found to be statistically significant in our specific analysis. Further caution against such a comparison is warranted due to the lack of a homogeneous analysis of the *Chandra* and *XMM-Newton* data. Finally, we obtain a non-zero intrinsic scatter at modest statistical significance and with a characteristic value of 2–5 keV from all three probes. This suggests that the ICM in MACS J0717.5+3745 is not isothermal, and the variations in temperature over the projected face of the cluster are likely attributable to the ongoing multiple merger.

While we caution against utilizing this present analysis as a tool to calibrate X-ray temperature measurements, we note that the rSZe does hold significant promise for obtaining such a calibration assessment. For instance, [Biffi et al. \(2014\)](#) find an on-average negligible bias between ICM temperatures obtained from different probes when restricting to morphologically regular clusters. Thus, an analysis based on a large sample of regular clusters would largely eliminate the potential astrophysical systematics related to ICM sub-structures noted above. In addition, the temperature of the ICM

in such clusters should fall within the energy bands of the X-ray satellites.

Looking to future spectrophotometric measurements of the SZe, this work has yielded some interesting insights. First, while FTS systems offer high spectral resolving power and potentially large mapping speeds, they are also very sensitive to mechanical and thermal changes that impact the optical path length while acquiring data. The SPIRE-FTS in particular was not designed to be sensitive to slowly varying continuum signals, and many of the low-frequency systematic effects in the data appear to be at least in part due to changes in the thermal properties of the instrument or the characteristics of the mechanical scanning mechanism. Optical systematic errors are also problematic in these measurements, with sensitivity to the precise temperature and configuration of the cold optics resulting in significant data loss. The inclusion of null data in the Dark Sky field to characterize these effects was crucial to extracting a scientific result from these observations. Secondly, as is made clear in Fig. 5, measurements of the rSZe should be optimized for bandwidths of ~ 50 GHz ($R \sim 15$) at sub-mm wavelengths. This would optimize sensitivity to the broad continuum signal produced by the SZe, while allowing sensitivity to the spectral features in the rSZe deviation that provide contrast to statistically constrain the temperature of the ICM. Finally, this case study highlights the need for accurate information about the sub-mm galaxies in the cluster field. The rSZe effect would have been buried beneath the CIB sources if we did not have high-sensitivity broadband information to subtract their contribution to the surface brightness.

While this very deep space-based FTS measurement is likely to remain unique for the foreseeable future, we did successfully extract the faint SZe signal from it. This demonstrates that interesting new measurements of the ICM using the rSZe effect are well within range of a sensitive next-generation instrument with carefully controlled systematics and modest spectral capability.

ACKNOWLEDGEMENTS

The authors sincerely thank I. Valtchanov for his assistance designing, executing, and understanding the SPIRE-FTS observations as our “Friend of the Observer” many years ago.

This work has been supported in part by the National Aeronautics and Space Administration under grants NAS7-03001-1467865, 80NSSC19K1018, and 80NSSC24K1024 and by the National Science Foundation under grants DGE-1745301 and NSF/AST-2206082. L. Lovisari acknowledges support from INAF

grant 1.05.24.05.15. The authors acknowledge Research Computing at the Rochester Institute of Technology for providing computational resources and support that have contributed to the research results reported in this publication.

The scientific results reported in this article are based in part on observations made with Herschel, a European Space Agency Cornerstone Mission with significant participation by NASA. HIPE is a joint development by the Herschel Science Ground Segment Consortium, consisting of ESA, the NASA Herschel Science Center, and the HIFI, PACS and SPIRE consortia. This research has made use of the NASA/IPAC Infrared Science Archive, which is funded by the National Aeronautics and Space Administration and operated by the California Institute of Technology.

Some of the data presented herein were obtained at the W. M. Keck Observatory, which is operated as a scientific partnership among the California Institute of Technology, the University of California, and NASA. The Observatory was made possible by the generous financial support of the W. M. Keck Foundation. The authors wish to recognize and acknowledge the very significant

cultural role and reverence that the summit of Maunakea has always had within the indigenous Hawaiian community. We are most fortunate to have the opportunity to conduct observations from this mountain.

The scientific results reported in this article are based in part on work at the Caltech Submillimeter Observatory, which is operated by the California Institute of Technology.

The scientific results reported in this article are based in part on observations obtained with XMM-*Newton*, an ESA science mission with instruments and contributions directly funded by ESA Member States and NASA.

The scientific results reported in this article are based in part on observations made by the Chandra X-ray Observatory.

Facility: Herschel, CSO, XMM, Chandra, Keck

Software: *astropy*, (Astropy Collaboration et al. 2013, 2018, 2022), SZpack (Chluba et al. 2012, 2013), emcee (Foreman-Mackey et al. 2013), PCAT (Feder et al. 2023), *scipy* (Virtanen et al. 2020), Xspec (Arnaud et al. 1999), Numpy (Harris et al. 2020), *contbin* (Sanders 2016), HIPE (Ott 2010), *matplotlib* (Hunter 2007), LMC

REFERENCES

- Adam, R., Bartalucci, I., Pratt, G. W., et al. 2017, *A&A*, 598, A115, doi: [10.1051/0004-6361/201629182](https://doi.org/10.1051/0004-6361/201629182)
- Arnaud, K., Dorman, B., & Gordon, C. 1999, XSPEC: An X-ray spectral fitting package, *Astrophysics Source Code Library*, record ascl:9910.005
- Arnaud, K. A. 1996, in *Astronomical Society of the Pacific Conference Series*, Vol. 101, *Astronomical Data Analysis Software and Systems V*, ed. G. H. Jacoby & J. Barnes, 17
- Arnaud, M., Pratt, G. W., Piffaretti, R., et al. 2010, *A&A*, 517, A92, doi: [10.1051/0004-6361/200913416](https://doi.org/10.1051/0004-6361/200913416)
- Asplund, M., Grevesse, N., Sauval, A. J., & Scott, P. 2009, *ARA&A*, 47, 481, doi: [10.1146/annurev.astro.46.060407.145222](https://doi.org/10.1146/annurev.astro.46.060407.145222)
- Astropy Collaboration, Robitaille, T. P., Tollerud, E. J., et al. 2013, *A&A*, 558, A33, doi: [10.1051/0004-6361/201322068](https://doi.org/10.1051/0004-6361/201322068)
- Astropy Collaboration, Price-Whelan, A. M., Sipőcz, B. M., et al. 2018, *AJ*, 156, 123, doi: [10.3847/1538-3881/aabc4f](https://doi.org/10.3847/1538-3881/aabc4f)
- Astropy Collaboration, Price-Whelan, A. M., Lim, P. L., et al. 2022, *ApJ*, 935, 167, doi: [10.3847/1538-4357/ac7c74](https://doi.org/10.3847/1538-4357/ac7c74)
- Beers, T. C., Flynn, K., & Gebhardt, K. 1990, *AJ*, 100, 32, doi: [10.1086/115487](https://doi.org/10.1086/115487)
- Benielli, D., Polehampton, E., Hopwood, R., et al. 2014, *Experimental Astronomy*, 37, 357, doi: [10.1007/s10686-013-9367-9](https://doi.org/10.1007/s10686-013-9367-9)
- Biffi, V., Sembolini, F., De Petris, M., et al. 2014, *MNRAS*, 439, 588, doi: [10.1093/mnras/stu018](https://doi.org/10.1093/mnras/stu018)
- Birkinshaw, M. 1999, *PhR*, 310, 97, doi: [10.1016/S0370-1573\(98\)00080-5](https://doi.org/10.1016/S0370-1573(98)00080-5)
- Birzan, L., Rafferty, D. A., McNamara, B. R., Wise, M. W., & Nulsen, P. E. J. 2004, *ApJ*, 607, 800, doi: [10.1086/383519](https://doi.org/10.1086/383519)
- Breuer, J. P., Werner, N., Plšek, T., et al. 2024, *arXiv e-prints*, arXiv:2411.08103, doi: [10.48550/arXiv.2411.08103](https://doi.org/10.48550/arXiv.2411.08103)
- Butler, V. L., Feder, R. M., Daylan, T., et al. 2022, *ApJ*, 932, 55, doi: [10.3847/1538-4357/ac6c04](https://doi.org/10.3847/1538-4357/ac6c04)
- Calzadilla, M. S., McDonald, M., Benson, B. A., et al. 2024, *ApJ*, 976, 169, doi: [10.3847/1538-4357/ad8916](https://doi.org/10.3847/1538-4357/ad8916)
- Cappellari, M., & Copin, Y. 2003, *MNRAS*, 342, 345, doi: [10.1046/j.1365-8711.2003.06541.x](https://doi.org/10.1046/j.1365-8711.2003.06541.x)
- Carlstrom, J. E., Holder, G. P., & Reese, E. D. 2002, *ARA&A*, 40, 643, doi: [10.1146/annurev.astro.40.060401.093803](https://doi.org/10.1146/annurev.astro.40.060401.093803)
- Cavagnolo, K. W., Donahue, M., Voit, G. M., & Sun, M. 2009, *ApJS*, 182, 12, doi: [10.1088/0067-0049/182/1/12](https://doi.org/10.1088/0067-0049/182/1/12)

- Chluba, J., Nagai, D., Sazonov, S., & Nelson, K. 2012, *MNRAS*, 426, 510, doi: [10.1111/j.1365-2966.2012.21741.x](https://doi.org/10.1111/j.1365-2966.2012.21741.x)
- Chluba, J., Switzer, E., Nelson, K., & Nagai, D. 2013, *MNRAS*, 430, 3054, doi: [10.1093/mnras/stt110](https://doi.org/10.1093/mnras/stt110)
- CXC-DS. 2002, Chandra X-ray Observatory ObsId 01655, Chandra X-ray Center/SAO, doi: [10.25574/01655](https://doi.org/10.25574/01655)
- Diehl, S., & Statler, T. S. 2006, *MNRAS*, 368, 497, doi: [10.1111/j.1365-2966.2006.10125.x](https://doi.org/10.1111/j.1365-2966.2006.10125.x)
- Dohlen, K., Origne, A., Pouliquen, D., & Swinyard, B. M. 2000, in *Society of Photo-Optical Instrumentation Engineers (SPIE) Conference Series*, Vol. 4013, UV, Optical, and IR Space Telescopes and Instruments, ed. J. B. Breckinridge & P. Jakobsen, 119–128, doi: [10.1117/12.393994](https://doi.org/10.1117/12.393994)
- Erler, J., Basu, K., Chluba, J., & Bertoldi, F. 2018, *MNRAS*, 476, 3360, doi: [10.1093/mnras/sty327](https://doi.org/10.1093/mnras/sty327)
- Feder, R. M., Butler, V., Daylan, T., et al. 2023, *AJ*, 166, 98, doi: [10.3847/1538-3881/ace69b](https://doi.org/10.3847/1538-3881/ace69b)
- Feder, R. M., Portillo, S. K. N., Daylan, T., & Finkbeiner, D. 2020, *AJ*, 159, 163, doi: [10.3847/1538-3881/ab74cf](https://doi.org/10.3847/1538-3881/ab74cf)
- Foreman-Mackey, D., Hogg, D. W., Lang, D., & Goodman, J. 2013, *PASP*, 125, 306, doi: [10.1086/670067](https://doi.org/10.1086/670067)
- Fulton, T., Naylor, D. A., Polehampton, E. T., et al. 2016, *MNRAS*, 458, 1977, doi: [10.1093/mnras/stw343](https://doi.org/10.1093/mnras/stw343)
- Gelman, A., & Rubin, D. B. 1992, *Statistical Science*, 7, 457, doi: [10.1214/ss/1177011136](https://doi.org/10.1214/ss/1177011136)
- Glenn, J., Ade, P. A. R., Amarie, M., et al. 2003, in *Society of Photo-Optical Instrumentation Engineers (SPIE) Conference Series*, Vol. 4855, Millimeter and Submillimeter Detectors for Astronomy, ed. T. G. Phillips & J. Zmuidzinas, 30–40, doi: [10.1117/12.459369](https://doi.org/10.1117/12.459369)
- Gonzalez, A. H., Zaritsky, D., & Zabludoff, A. I. 2007, *ApJ*, 666, 147, doi: [10.1086/519729](https://doi.org/10.1086/519729)
- Griffin, M. J., Abergel, A., Abreu, A., et al. 2010, *A&A*, 518, L3, doi: [10.1051/0004-6361/201014519](https://doi.org/10.1051/0004-6361/201014519)
- Harris, C. R., Millman, K. J., van der Walt, S. J., et al. 2020, *Nature*, 585, 357, doi: [10.1038/s41586-020-2649-2](https://doi.org/10.1038/s41586-020-2649-2)
- Harrison, F. A., Craig, W. W., Christensen, F. E., et al. 2013, *ApJ*, 770, 103, doi: [10.1088/0004-637X/770/2/103](https://doi.org/10.1088/0004-637X/770/2/103)
- HI4PI Collaboration, Ben Bekhti, N., Flöer, L., et al. 2016, *A&A*, 594, A116, doi: [10.1051/0004-6361/201629178](https://doi.org/10.1051/0004-6361/201629178)
- Hopwood, R., Polehampton, E. T., Valtchanov, I., et al. 2015, *MNRAS*, 449, 2274, doi: [10.1093/mnras/stv353](https://doi.org/10.1093/mnras/stv353)
- Hudson, D. S., Mittal, R., Reiprich, T. H., et al. 2010, *A&A*, 513, A37, doi: [10.1051/0004-6361/200912377](https://doi.org/10.1051/0004-6361/200912377)
- Hunter, J. D. 2007, *Computing in Science and Engineering*, 9, 90, doi: [10.1109/MCSE.2007.55](https://doi.org/10.1109/MCSE.2007.55)
- Hurier, G., & Tchernin, C. 2017, *A&A*, 604, A94, doi: [10.1051/0004-6361/201629993](https://doi.org/10.1051/0004-6361/201629993)
- Itoh, N., Kohyama, Y., & Nozawa, S. 1998, *ApJ*, 502, 7, doi: [10.1086/305876](https://doi.org/10.1086/305876)
- Jansen, F., Lumb, D., Altieri, B., et al. 2001, *A&A*, 365, L1, doi: [10.1051/0004-6361:20000036](https://doi.org/10.1051/0004-6361:20000036)
- Kravtsov, A. V., & Borgani, S. 2012, *ARA&A*, 50, 353, doi: [10.1146/annurev-astro-081811-125502](https://doi.org/10.1146/annurev-astro-081811-125502)
- Kuntz, K. D., & Snowden, S. L. 2008, *A&A*, 478, 575, doi: [10.1051/0004-6361:20077912](https://doi.org/10.1051/0004-6361:20077912)
- Lee, E., Anbajagane, D., Singh, P., et al. 2022, *MNRAS*, 517, 5303, doi: [10.1093/mnras/stac2781](https://doi.org/10.1093/mnras/stac2781)
- Lin, Y.-T., Stanford, S. A., Eisenhardt, P. R. M., et al. 2012, *ApJL*, 745, L3, doi: [10.1088/2041-8205/745/1/L3](https://doi.org/10.1088/2041-8205/745/1/L3)
- Lovisari, L., & Reiprich, T. H. 2019, *MNRAS*, 483, 540, doi: [10.1093/mnras/sty3130](https://doi.org/10.1093/mnras/sty3130)
- Lovisari, L., Etti, S., Rasia, E., et al. 2024, *A&A*, 682, A45, doi: [10.1051/0004-6361/202346651](https://doi.org/10.1051/0004-6361/202346651)
- Ma, C.-J., Ebeling, H., & Barrett, E. 2009, *ApJL*, 693, L56, doi: [10.1088/0004-637X/693/2/L56](https://doi.org/10.1088/0004-637X/693/2/L56)
- Mantz, A. B. 2016, *MNRAS*, 457, 1279, doi: [10.1093/mnras/stv3008](https://doi.org/10.1093/mnras/stv3008)
- Marchili, N., Hopwood, R., Fulton, T., et al. 2017, *MNRAS*, 464, 3331, doi: [10.1093/mnras/stw2600](https://doi.org/10.1093/mnras/stw2600)
- Markevitch, M. 2006, in *ESA Special Publication*, Vol. 604, *The X-ray Universe 2005*, ed. A. Wilson, 723, doi: [10.48550/arXiv.astro-ph/0511345](https://doi.org/10.48550/arXiv.astro-ph/0511345)
- Markevitch, M., & Vikhlinin, A. 2007, *PhR*, 443, 1, doi: [10.1016/j.physrep.2007.01.001](https://doi.org/10.1016/j.physrep.2007.01.001)
- Mroczkowski, T., Nagai, D., Basu, K., et al. 2019, *SSRv*, 215, 17, doi: [10.1007/s11214-019-0581-2](https://doi.org/10.1007/s11214-019-0581-2)
- Naylor, D. A., Gom, B. G., Schofield, I., Tompkins, G., & Davis, G. R. 2003, in *Society of Photo-Optical Instrumentation Engineers (SPIE) Conference Series*, Vol. 4855, *Millimeter and Submillimeter Detectors for Astronomy*, ed. T. G. Phillips & J. Zmuidzinas, 540–551, doi: [10.1117/12.459108](https://doi.org/10.1117/12.459108)
- Naylor, D. A., Baluteau, J.-P., Bendo, G. J., et al. 2014, in *Space Telescopes and Instrumentation 2014: Optical, Infrared, and Millimeter Wave*, ed. J. M. O. Jr., M. Clampin, G. G. Fazio, & H. A. MacEwen, Vol. 9143, *International Society for Optics and Photonics (SPIE)*, 91432D, doi: [10.1117/12.2054989](https://doi.org/10.1117/12.2054989)
- Ott, S. 2010, in *Astronomical Society of the Pacific Conference Series*, Vol. 434, *Astronomical Data Analysis Software and Systems XIX*, ed. Y. Mizumoto, K. I. Morita, & M. Ohishi, 139, doi: [10.48550/arXiv.1011.1209](https://doi.org/10.48550/arXiv.1011.1209)
- Pearson, C., Varnish, T. W. O., Wu, X., et al. 2025, *MNRAS*, 539, 336, doi: [10.1093/mnras/staf335](https://doi.org/10.1093/mnras/staf335)
- Planck Collaboration, Ade, P. A. R., Aghanim, N., et al. 2011, *A&A*, 536, A18, doi: [10.1051/0004-6361/201116461](https://doi.org/10.1051/0004-6361/201116461)

- Planck Collaboration, Abergel, A., Ade, P. A. R., et al. 2014, *A&A*, 571, A11, doi: [10.1051/0004-6361/201323195](https://doi.org/10.1051/0004-6361/201323195)
- Planck Collaboration, Adam, R., Ade, P. A. R., et al. 2016, *A&A*, 596, A104, doi: [10.1051/0004-6361/201628522](https://doi.org/10.1051/0004-6361/201628522)
- Planck Team. 2015, Planck Public Data Release 2 BOLOCAM Galaxy Cluster Archive, IPAC, doi: [10.26131/IRSA562](https://doi.org/10.26131/IRSA562)
- Remazeilles, M. 2022, in *European Physical Journal Web of Conferences*, Vol. 257, mm Universe @ NIKA2 - Observing the mm Universe with the NIKA2 Camera, 00040, doi: [10.1051/epjconf/202225700040](https://doi.org/10.1051/epjconf/202225700040)
- Remazeilles, M., & Chluba, J. 2025, *MNRAS*, 538, 1576, doi: [10.1093/mnras/staf384](https://doi.org/10.1093/mnras/staf384)
- Rhea, C., Hlavacek-Larrondo, J., Perreault-Levasseur, L., Gendron-Marsolais, M.-L., & Kraft, R. 2020, *AJ*, 160, 202, doi: [10.3847/1538-3881/abb468](https://doi.org/10.3847/1538-3881/abb468)
- Rossetti, M., & Molendi, S. 2010, *A&A*, 510, A83, doi: [10.1051/0004-6361/200913156](https://doi.org/10.1051/0004-6361/200913156)
- Sabol, E. J., & Snowden, S. L. 2019, *sxrbg: ROSAT X-Ray Background Tool*, *Astrophysics Source Code Library*, record ascl:1904.001
- Sanders, J. S. 2016, *contbin: Contour binning and accumulative smoothing*, *Astrophysics Source Code Library*, record ascl:1609.023
- Sarazin, C. L. 1986, *Reviews of Modern Physics*, 58, 1, doi: [10.1103/RevModPhys.58.1](https://doi.org/10.1103/RevModPhys.58.1)
- Sayers, J., Mroczkowski, T., Zemcov, M., et al. 2013, *ApJ*, 778, 52, doi: [10.1088/0004-637X/778/1/52](https://doi.org/10.1088/0004-637X/778/1/52)
- Sayers, J., Montaña, A., Mroczkowski, T., et al. 2019, *ApJ*, 880, 45, doi: [10.3847/1538-4357/ab29ef](https://doi.org/10.3847/1538-4357/ab29ef)
- Schellenberger, G., Reiprich, T. H., Lovisari, L., Nevalainen, J., & David, L. 2015, *A&A*, 575, A30, doi: [10.1051/0004-6361/201424085](https://doi.org/10.1051/0004-6361/201424085)
- Silich, E. M., Bellomi, E., Sayers, J., et al. 2024, *ApJ*, 968, 74, doi: [10.3847/1538-4357/ad3fb5](https://doi.org/10.3847/1538-4357/ad3fb5)
- Smith, R. K., Brickhouse, N. S., Liedahl, D. A., & Raymond, J. C. 2001, *ApJL*, 556, L91, doi: [10.1086/322992](https://doi.org/10.1086/322992)
- Sunyaev, R. A., & Zeldovich, Y. B. 1972, *Comments on Astrophysics and Space Physics*, 4, 173
- Suzuki, H., Plucinsky, P. P., Gaetz, T. J., & Bamba, A. 2021, *A&A*, 655, A116, doi: [10.1051/0004-6361/202141458](https://doi.org/10.1051/0004-6361/202141458)
- Swinyard, B. M., Ade, P., Baluteau, J. P., et al. 2010, *A&A*, 518, L4, doi: [10.1051/0004-6361/201014605](https://doi.org/10.1051/0004-6361/201014605)
- Valtchanov, I. 2018, *The Spectral and Photometric Imaging Receiver (SPIRE) Handbook*, Tech. Rep. HERSCHEL-HSC-DOC-0798, v 3.2, Herschel Explanatory Supplement Vol. IV, European Space Agency
- Valtchanov, I., Hopwood, R., Bendo, G., et al. 2018, *MNRAS*, 475, 321, doi: [10.1093/mnras/stx3178](https://doi.org/10.1093/mnras/stx3178)
- Vikhlinin, A., Kravtsov, A., Forman, W., et al. 2006, *ApJ*, 640, 691, doi: [10.1086/500288](https://doi.org/10.1086/500288)
- Virtanen, P., Gommers, R., Oliphant, T. E., et al. 2020, *Nature Methods*, 17, 261, doi: [10.1038/s41592-019-0686-2](https://doi.org/10.1038/s41592-019-0686-2)
- Weisskopf, M. C., Tananbaum, H. D., Van Speybroeck, L. P., & O'Dell, S. L. 2000, in *Society of Photo-Optical Instrumentation Engineers (SPIE) Conference Series*, Vol. 4012, *X-Ray Optics, Instruments, and Missions III*, ed. J. E. Truemper & B. Aschenbach, 2–16, doi: [10.1117/12.391545](https://doi.org/10.1117/12.391545)
- Wik, D. R., Hornstrup, A., Molendi, S., et al. 2014, *ApJ*, 792, 48, doi: [10.1088/0004-637X/792/1/48](https://doi.org/10.1088/0004-637X/792/1/48)
- Willingale, R., Starling, R. L. C., Beardmore, A. P., Tanvir, N. R., & O'Brien, P. T. 2013, *MNRAS*, 431, 394, doi: [10.1093/mnras/stt175](https://doi.org/10.1093/mnras/stt175)
- Wright, E. L. 1979, *ApJ*, 232, 348, doi: [10.1086/157294](https://doi.org/10.1086/157294)
- Zemcov, M., Rex, M., Rawle, T. D., et al. 2010, *A&A*, 518, L16, doi: [10.1051/0004-6361/201014685](https://doi.org/10.1051/0004-6361/201014685)
- Zemcov, M., Aguirre, J., Bock, J., et al. 2012, *ApJ*, 749, 114, doi: [10.1088/0004-637X/749/2/114](https://doi.org/10.1088/0004-637X/749/2/114)